From: FNALD::CAROL 29-JAN-1994 13:55:46.38
To: @CDF_ELECT_DIST.DIS
CC:
Subj: CDF Note No. 2443 Available as a PostScript File (CDFNOTE_2443.PS)

January 29, 1994

Dear CDF Collaborators,

CDF Note No. 2443 is ready for electronic distribution. The PostScript file can be found and printed:

CDF$PUB:CDFNOTE_2443.PS

CDF Note No. 2443 describes the properties of multijet events with large total transverse energies recorded in our Run 1a Stream 2 high-sumet data sample. The physics plots in this note will be offered for blessing during a coming Friday meeting, so that the results will be available for presentation in the coming conferences.

Steve Geer

CDF/DOC/JET/CDFR/2443
27th January 1994

Properties of Multijet Events with Large Total Transverse Energies at the Fermilab Proton-Antiproton Collider

S. Geer

Fermi National Acccelerator Laboratory
P.O. Box 500, Batavia, Illinois 60510

Abstract

The properties of multijet events with large total transverse energies and high multijet masses are compared with leading order perturbative QCD expectations. The jet multiplicity distribution extends up to ten jets with $E_T > 20$ GeV. The HERWIG QCD parton shower Monte Carlo correctly predicts the fraction of events with two-, three-, four-, and five-jets. HERWIG also gives a good description of the multijet mass distributions and describes the angular distributions of the leading jets in the N-body rest frames. However, the HERWIG Monte Carlo underestimates the fraction of events with more than five jets, and the discrepancy increases with increasing jet multiplicity. Furthermore, HERWIG does not give a good description of the jet transverse momentum spectra for three-jet and four-jet events. We believe that these discrepancies reflect the limitations of the parton shower Monte Carlo which is based on the leading order $2 \rightarrow 2$ matrix element plus gluon radiation. We have therefore also compared the data with the complete leading order $2 \rightarrow N$ matrix element calculations embodied in the NJETS Monte Carlo. This calculation is also able to describe the multijet mass and angular distributions, and gives a better description than HERWIG of the jet transverse momentum distribution in three-jet events. This may indicate that our data tests the QCD matrix elements at a deeper level than the parton shower Monte Carlo approximation.

1 INTRODUCTION

During the 1992/3 proton-antiproton collider run CDF recorded data corressponding to an integrated luminosity of 21 pb^{-1}. This note describes an analysis of multijet events with $\sum E_T > 420$ GeV. These spectacular events produced in proton-antiproton collisions at $\sqrt{s}$ = 1.8 TeV enable us to test perturbative QCD and search for new phenomena in a region of parameter space which has not been previously explored; namely at large parton x and Q^2 with many (up to 10) hard partons in the final state.

Within the framework of perturbative QCD, events with large $\sum E_T$ arise from hard scattering of the constituent partons in the proton and antiproton. The outgoing scattered partons manifest themselves as hadronic jets. The resulting events are therefore expected to contain two jets with large components of momenta transverse to the beam directions (p_T). Higher order QCD corrections to the basic parton-parton scattering process can give rise to additional high-p_T jets in the final state, resulting in more complicated event toplogies.

Two-jet, three-jet, and four-jet topologies have been analysed previously both at the CERN proton-antiproton collider, and by CDF using the 1988/9 Fermilab collider data. In this note we present the jet multiplicity distribution, describe the events with the largest jet multiplicities, and and compare with QCD expectations the observed two-jet, three-jet, four-jet, five-jet, and six-jet mass- and angular- distributions.

2 Data Sample

A description of the high $\sum E_T$ trigger, and the offline cuts used to define the data sample, can be found in ref.[1]. The following is a summary of the trigger and event selection requirements.

2.1 Level 2 Trigger

The high-$\sum E_T$ trigger required:

$$\sum E_T > 175 \text{ GeV} \tag{1}$$

where the sum is over all uncorrected calorimeter clusters with $E_T > 10$ GeV in the central, plug and forward calorimeters, and the level 2 clusters consist of a seed tower with $E_T > 3$ GeV and all contiguous towers with $E_T > 1$ GeV.

2.2 Level 3 Trigger

At level 3 the high-$\sum E_T$ stream 2 data sample was selected by requiring:

$$\sum E_T > 300 \text{ GeV}, \tag{2}$$

where the sum is over all calorimeter clusters with $E_T > 10$ GeV reconstructed with the CDF jet clustering algorithm[2] using a cone size $\triangle R = 0.7$. Transverse energies were computed assuming that the event vertex was at z = 0. Cosmic rays, beam halo, and calorimeter malfunctions were supressed by rejecting events where both (i) the fraction of the total energy in the electromagnetic calorimeters is less than 0.2, AND (ii) the $\not\!\!E_T$ significance [3]:

$$S \equiv \not\!\!E_T / \left(\sum E_T\right)^{1/2} > 10. \tag{3}$$

A total of 18322 events in the 1992/3 run passed the level 3 high-$\sum E_T$ selection.

2.3 Offline Selection

To further reject cosmic rays, beam halo, and calorimeter malfunctions, events are rejected if:

(i) There is significant energy deposited in the hadron calorimeter out of time with the proton-antiproton collision (HATFLT).

(ii) The total energy exceeds 2000 GeV.

(iii) There is no reconstructed primary vertex with $\mid z \mid < 60$ cm.

(iv) S > 6 (corressponding to $\not\!\!E_T > 104$ GeV for an event with $\sum E_T > 300$ GeV).

Finally, we wish to select events based on their calculated total transverse energies after the reconstructed jets have been corrected with JTC90S (the offline 6.1 version of the jet correction routine QDJSCO). Figure 1 shows the distribution of corrected $\sum E_T$ before cutting on this quantity. The sum is over all corrected jets with corrected $E_T > 20$ GeV. Note that above the turn-on the distribution is reasonably well described by an exponential function. To ensure that we are fully efficient above the final $\sum E_T$ cut we require:

$$\sum E_T > 420 \; GeV. \tag{4}$$

A total of 4632 events pass these requirements.

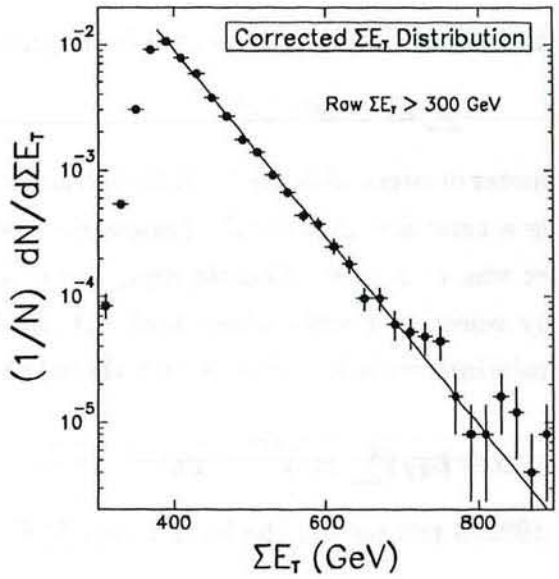

Figure 1: Distribution of corrected total transverse energy for events before the final cut on this quantity (points) compared with an exponential fit (curve).

3 QCD Predictions

To compare observed distributions with QCD expectations we will use the following:

(i) Leading Order (LO) parton-level $2 \rightarrow N$ matrix element calculations (NJETS) together with a Gaussian experimental jet energy resolution function.

(ii) LO $2 \rightarrow 2$ parton shower Monte Carlo (HERWIG) predictions together with a full simulation of the CDF detector (QFL).

(iii) Analytical forms for the LO predictions, or approximations to them, where available.

3.1 NJETS

The NJETS program provides LO QCD parton-level calculations of the $2 \rightarrow N$ matrix elements. In this note NJETS results are presented for $2 \rightarrow 2$ and $2 \rightarrow 3$ processes. A $2 \rightarrow 4$ calculation is in progress. In the future it is hoped that predictions from the NJETS $2 \rightarrow 5$ calculation will also be available. The MRSD0 structure functions have been used for all of our NJETS calculations with the Q^2 scale given by the average jet E_T . The predictions are

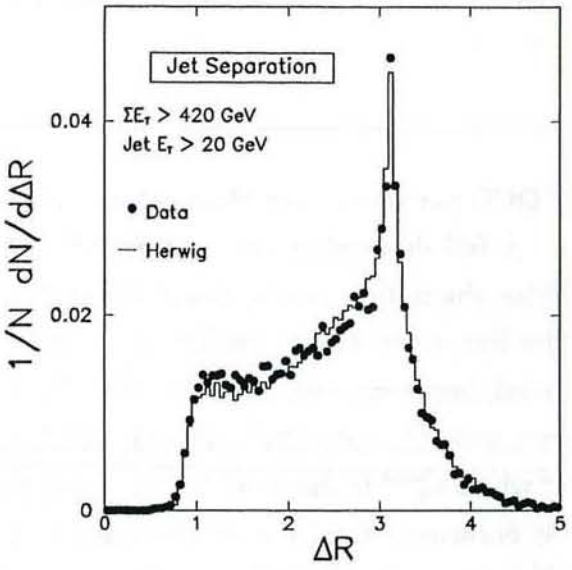

Figure 2: Distribution of jet separations for data (points) and HERWIG (histogram).

for summed parton $E_T > 420$ GeV, where the parton transverse energies have been smeared by the Gaussian resolution function:

$$\sigma_{E_T} = 0.1\ E_T \tag{5}$$

The NJETS predictions assume that jets are reconstructed if the underlying hard partons have:

(i) $E_T > 20$ GeV,

(ii) $|\eta| < 3$, and

(iii) $\Delta R(j,j) > \Delta R_{MIN} = 1.0$.

The value $\Delta R_{MIN} = 1.0$ was chosen because the observed distribution of jet separations (Fig. 2) has a cutoff at this value. The advantages of the NJETS approach are (a) the predictions are a direct consequence of the $2 \rightarrow$ N QCD matrix elements, and (b) the numerical integrations that are performed are less CPU intensive and the statistical precision of the predictions is less of a limitaion than for more complete calculations incorporating a full detector simulation. The disadvantage of the NJETS approach is that the predictions do

not take account of the full details of the detector, parton hadronization, or the underlying event.

3.2 HERWIG

HERWIG [4] is a leading-order QCD parton shower Monte Carlo that includes both initial and final-state gluon radiation. A full description of the HERWIG Monte Carlo together with details of the (QFL) detector simulation can be found in ref.[5]. Our HERWIG predictions can be thought of as leading-order $2 \rightarrow 2$ predictions with gluon radiation, color coherence, hadronization, an underlying event, and a full detector simulation. We have used the CTEQ1M structure functions and $Q^2 = stu/2(s^2+u^2+t^2)$. HERWIG generates $2 \rightarrow 2$ processes above a specified p_T^{hard} where p_T^{hard} is the p_T of the outgoing partons from the hard scatter before any radiation has occurred. We have set the minimum p_T^{hard} to 60 GeV/c. This relatively low value of p_T^{hard} is necessary to obtain an unbiased Monte Carlo sample in which adequate account is taken of events in which the detector response has fluctuated upwards by several standard deviations and/or the spectator system, including the initial-state radiation, makes an unusually large contribution to the $\sum E_T$. This low value necessitates generating a large number of events in order to get one event that has high $\sum E_T$ (only 0.2% of the events generated have uncorrected $\sum E_T > 300$ GeV). The Monte Carlo sample corresponds to an integrated luminosity of 10 pb^{-1}.

3.3 Analytical Predictions

In the center-of-mass system, the distribution of parton-parton scattering angles $\theta^\star$ is expected to be given approximately by the Rutherford Scattering form :

$$\frac{d\sigma}{d\cos\theta^\star} \sim (1 - \cos\theta^\star)^{-2}. \tag{6}$$

The LO QCD calculations predict deviations from Rutherford scattering. The LO $2 \rightarrow 2$ matrix elements can be expressed as a function of the angular variable :

$$\chi \equiv \frac{1 + \cos\theta^\star}{1 - \cos\theta^\star} = \frac{\hat{u}}{\hat{t}}. \tag{7}$$

Parton Subprocess	$f_i(\chi)$
$q_1 q_1 \to q_1 q_1$	$\frac{8}{9}\left[F(\chi) - \frac{1}{3}(\chi + 2 + \chi^{-1})\right]$
$q_1 \overline{q_1} \to q_1 \overline{q_1}$	$\frac{8}{9}\left[F(\chi) + \frac{1}{3}(\chi - 1 + \chi^{-1}) + \frac{\chi^2+1}{(\chi+1)^2}\right]$
$qg \to qg$	$2\left[F(\chi) + \frac{4}{9}\left(\frac{1}{2}\chi + \frac{3}{2} + \frac{1}{2}\chi^{-1}\right)\right]$
$gg \to gg$	$\frac{9}{2}\left[F(\chi) + 2 - \frac{\chi}{(1+\chi)^2}\right]$

Table 1: Angular dependence of leading order QCD parton-parton subprocess cross-sections.

The angular dependence of the parton-parton scattering matrix elements is given approximately by :

$$\frac{d\sigma}{d\chi} \sim \frac{F(\chi)}{(1+\chi)^2}, \tag{8}$$

where

$$F(\chi) \equiv \chi^2 + \chi + 1 + \frac{1}{\chi} + \frac{1}{\chi^2}. \tag{9}$$

More precisely, the exact form of the matrix element depends on the parton-parton subprocesses. The angular dependences for the various subprocesses i are given by:

$$\frac{d\sigma}{d\chi} \sim \frac{f_i(\chi)}{(1+\chi)^2} \tag{10}$$

or

$$\frac{d\sigma}{d\cos\theta^*} \sim \frac{f_i(\chi)}{(1+\chi)^2}\left[\frac{2}{(1-\cos\theta^*)^2}\right], \tag{11}$$

where $f_i(\chi)$ are listed in Table 1, and the similarity of the LO $2 \to 2$ subprocess angular distributions to the Rutherford scattering form is shown in Fig. 3.

3.4 Theoretical Prejudice

We have some theoretical prejudice that will guide us in the way we analyse the data, and which we can test experimentally:

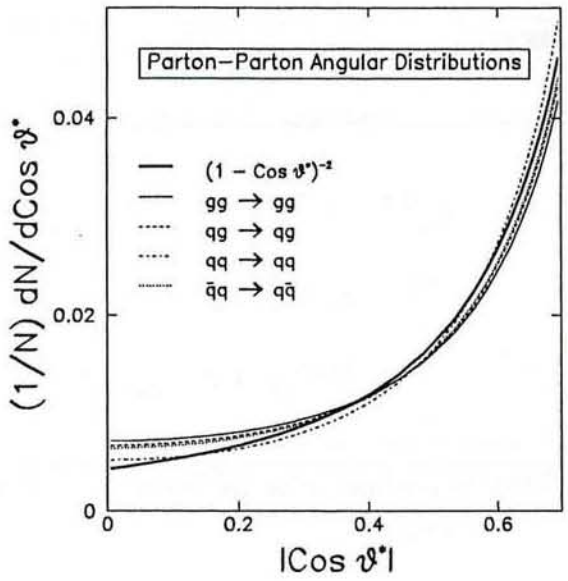

Figure 3: Expectations for subprocess angluar distributions (Table 1) for quark-antiquark, quark-gluon, and gluon-gluon scattering. The solid curve shows the expectation for Rutherford scattering.

(a) We speculate that the mass- and angular-dependence of the multijet differential cross-sections approximately factorize .. the mass-dependence predominantly reflecting the rapidly falling structure functions at high x, and the angular dependence approximately given by $F(\chi) / (1+\chi)^2$. In detail we do expect some mass-dependence of the angular distributions since the parton-parton subprocess mix changes with subprocess center-of-mass energy. Since the subprocess angular distributions are very similar, we expect this to be a small effect. Noting that at fixed angle, Q^2 increases with increasing two-jet mass, we also expect some dependence of the angular distribution on mass due to the running of the strong coupling constant $\alpha_S(Q^2)$. Again, we expect this to be a small effect.

(b) We speculate that N-jet mass- and angular-distributions ($N > 2$) are similar to the two-jet distributions. We owe this prejudice to the knowledge that in our previous high-$\sum E_T$ analysis[5] we observed that the HERWIG predictions gave a good description of many features of the data, which suggests that $2 \rightarrow 2$ scattering plus gluon radiation gives a good first approximation to reality.

4 Jet Multiplicity Distribution

For the analysis described in this note, jets have been reconstructed with the CDF jet algorithm using a cone size $\Delta R = 0.7$, and the jet four-vectors have been corrected using JTC90S. Jets are retained if their corrected $E_T > 20$ GeV.

N_J	*Events*	*Events* ($\cos\theta^\star < 0.67, m > 600\,GeV$)
2	1302	188
3	1595	308
4	1105	274
5	436	129
6	141	38
7	36	8
8	14	2
9	2	0
10	1	0
Total	4632	947

Table 2: Jet multiplicity distribution for jets with corrected $E_T > 20$ GeV. The right-most column shows the multiplicity distribution after cutting on the multijet mass and leading-jet center-of-mass scattering angle as indicated.

The resulting jet multiplicity distribution is tabulated in Table 2 and compared with HERWIG predictions in Fig. 4. HERWIG gives a remarkably good description of the fraction of events with two-jets, three-jets, four-jets, and five-jets. This suggests that for these topologies LO $2 \to 2$ scattering plus hard gluon radiation gives a good first approximation to the data. HERWIG underestimates the observed fraction of events with jet multiplicities larger than five, and the discrepency increases with increasing jet multiplicity. We suspect that this reflects a limitiation of the HERWIG predictions. Note that a similar effect has been observed in comparing HERWIG predictions for W + N-jet production with complete LO calculations[6]. Compared with the complete LO calculation, the parton shower Monte Carlo underestimates the rate for large N.

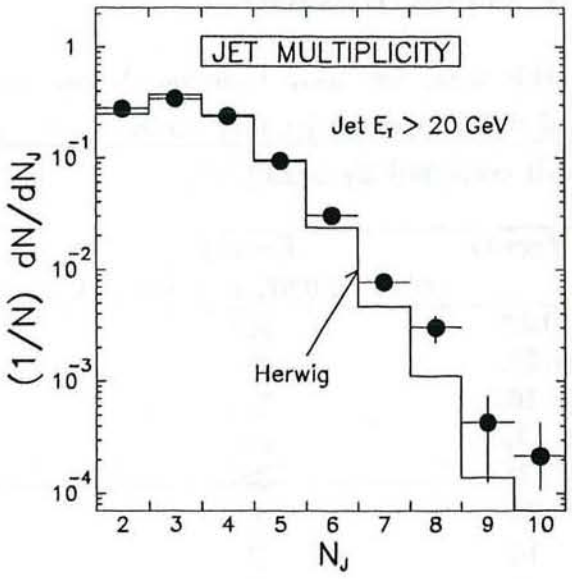

Figure 4: Jet multiplicity distribution. Data (points) compared with HERWIG + QFL predictions (histogram). Jets have been reconstructed with a cone size $\triangle R = 0.7$ and retained if the corrected jet E_T exceeds 20 GeV.

5 Exclusive Two-Jet Analysis

In the two-jet rest-frame, at fixed two-jet mass there is a maximum value of $\cos\theta^*$ that is consistent with the $\sum E_T > 420$ GeV requirement. The maximum value of $\cos\theta^*$ is given by:

$$\cos\theta^*_{MAX} = \sqrt{\left[1 - \left(\frac{420}{m_{2J}}\right)^2\right]}. \tag{12}$$

The mass dependence of $\cos\theta^*_{MAX}$ is shown in Fig. 5. For simplicity, we will compare data with QCD expectactions within the region $\cos\theta^* < 0.67$ and $m_{2J} < 600$ GeV, which is shown in the figure to be safely contained within the fully efficient region. This minimizes uncertainties due to imprecise modelling of the acceptance close to the bound. Unfortunately only 14% (188 events) of the two-jet events are within the large mass and large scattering angle region. The distribution of $\cos\theta^*$ versus mass is shown in Fig. 6 for two-jet events. The data are clearly suppressed above the $\cos\theta^*_{MAX}$ bound.

The two-jet mass distribution is compared in Fig. 7 with QCD predictions for events with $\sum E_T > 420$ GeV, and $|\cos\theta^*| < 0.67$. The distribution extends up to masses of 1 TeV, and

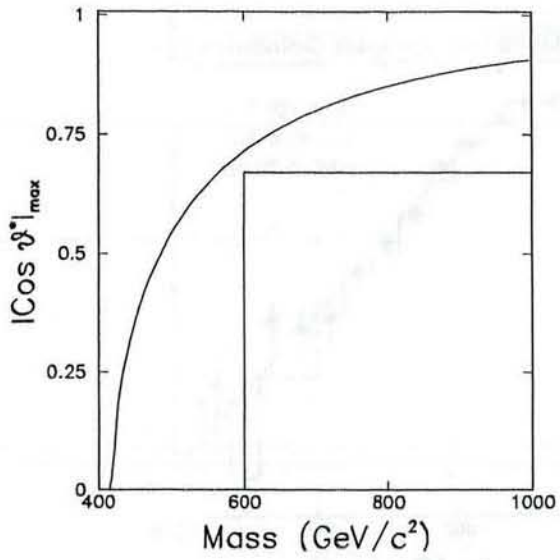

Figure 5: Maximum value of $\cos\theta^\star$ consistent with the minimum $\sum E_T$ requirement shown as a function of two-jet mass (curve). The box shows the region $\cos\theta^\star < 0.67$ and $m_{2J} > 600$ GeV is fully contained within the $\cos\theta^\star_{MAX}$ boundary.

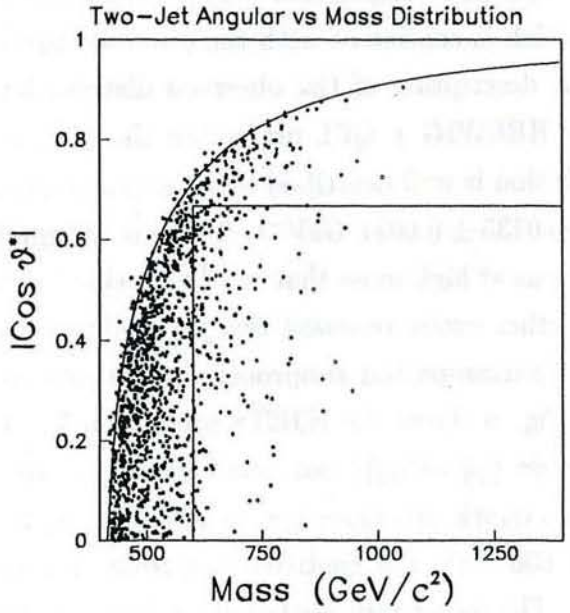

Figure 6: Distribution of $\cos\theta^\star$ versus mass for two-jet events. The curve shows, as a function of mass, the maximum value of $\cos\theta^\star$ consistent with the minimum $\sum E_T$ requirement. The box shows the region $\cos\theta^\star < 0.67$ and $m > 600$ GeV.

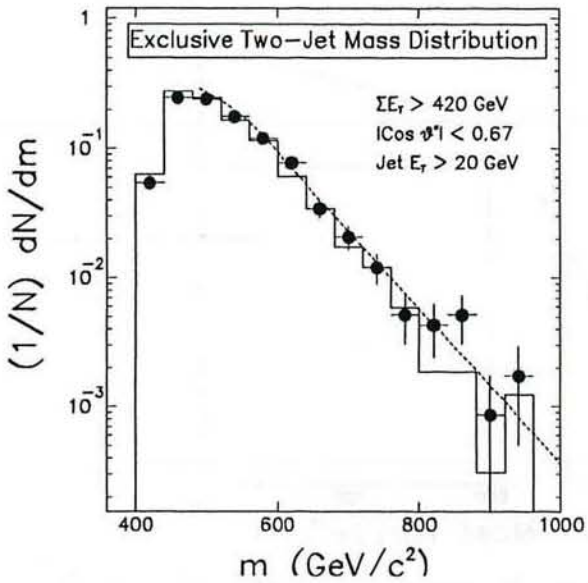

Figure 7: Two-Jet mass distribution. Data (points) compared with HERWIG (histogram) and NJETS (broken line) predictions.

turns over a little below $m = 600$ GeV. Expression (12) predicts that the inefficient region will start at $m = 566$ GeV, which is consistent with the observed turn-on. Both HERWIG and NJETS give a reasonable description of the observed distribution above the turn-on region ($m_{2J} > 600$ GeV). The HERWIG + QFL prediction also gives a good description of the turn-on. The mass-distribution is well described by an exponential distribution (Fig. 8) with a slope parameter $b = -0.0135 \pm 0.0011\ GeV^{-1}$. There is no significant evidence for a deviation from QCD expectations at high mass that can be ascribed to parton-substructure, Axigluons, excited quarks, or other exotic resonant two-jet production.

It is worth noting that the parton-parton subprocess mix is expected to change significantly with increasing mass: Fig. 9 shows the NJETS prediction for the fraction of events arising from four-quark processes ($q\overline{q} \rightarrow q\overline{q}$), two-quark processes (qg $\rightarrow$ qg, $\overline{q}$g $\rightarrow$ $\overline{q}$g, $q\overline{q}$ $\rightarrow$ gg, and gg $\rightarrow$ $q\overline{q}$), and zero-quark processes (gg $\rightarrow$ gg). For m > 600 GeV the gg $\rightarrow$ gg contribution is small. At 600 GeV the contributions from two-quark and four-quark subprocesses are about equal. The four-quark contribution increases with increasing mass, until at 1 TeV the $q\overline{q} \rightarrow q\overline{q}$ subprocess is expected to contribute about 80% of the two-jet cross-section. The agreement between the observed and predicted two-jet mass distributions

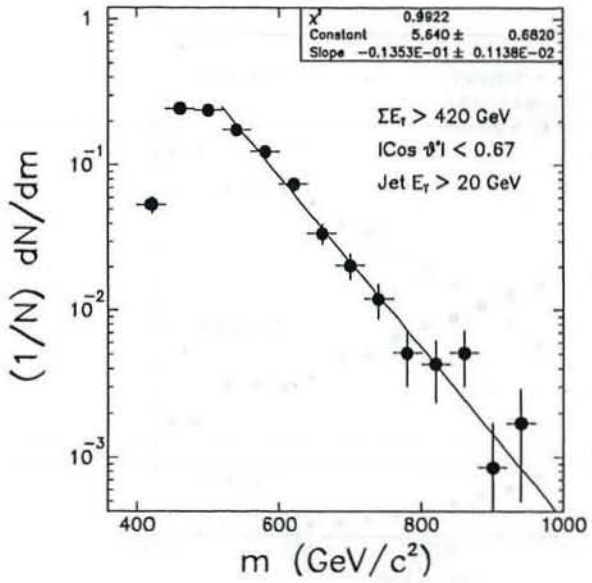

Figure 8: Exponential fit to the exclusive two-jet mass spectrum.

therefore provides an indirect check that the relative contributions from the various $2 \to 2$ subprocesses are well described by the theory.

The observed two-jet angular distribution is compared with HERWIG and NJETS predictions in Fig. 10. Both QCD predictions give a reasonable description of the data, as indeed does Rutherford scattering. We conclude that the two-jet data at high-$\sum E_T$ are described more-or-less equally well by both the LO QCD matrix element calculation and by the LO $2 \to 2$ Monte Carlo calculation including gluon radiation, the detector simulation etc. Furthermore, the data are also well described by the Rutherford scattering form for the angular distribution, and a simple exponentially falling mass distribution. Hence, although LO perturbative QCD gives an adequate description of the two-jet mass- and angular-distributions, this appears to be a somewhat limited test of the theory; we suspect that the mass distribution primarilly reflects the rapidly falling parton-distributions at high x, and the angular distribution primarilly reflects the approximate Rutherford Scattering form of the LO parton-parton matrix elements.

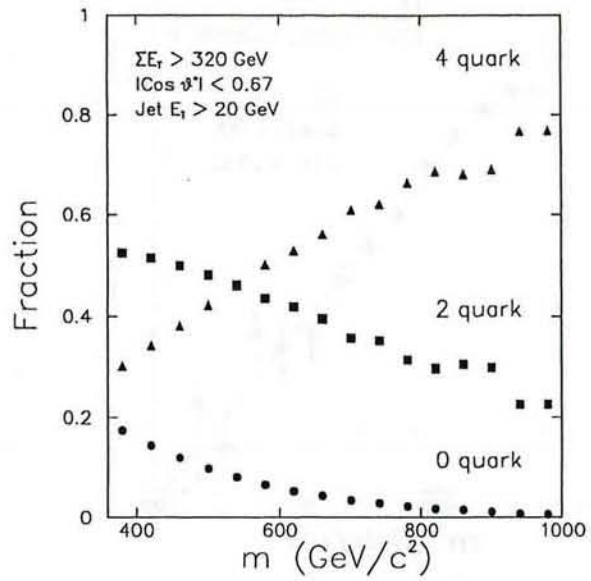

Figure 9: NJETS predictions for the subprocess fractions as a function of two-jet mass.

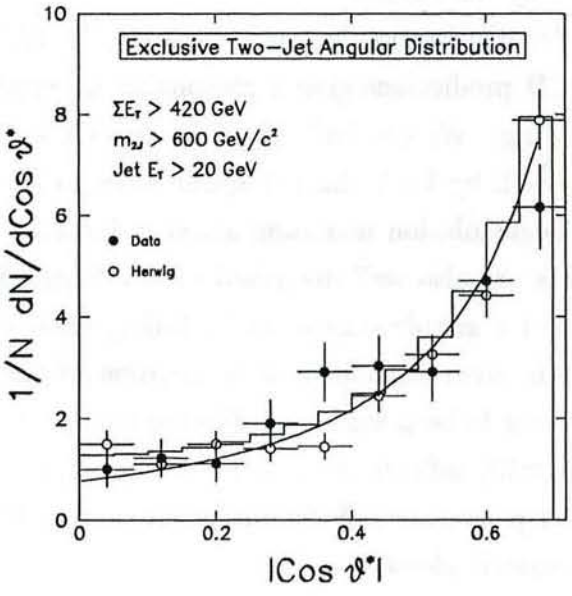

Figure 10: Two-jet angular distribution. Data (solid points) compared with HERWIG (open points) predictions, NJETS (histogram) predictions, and the Rutherford scattering form (broken curve).

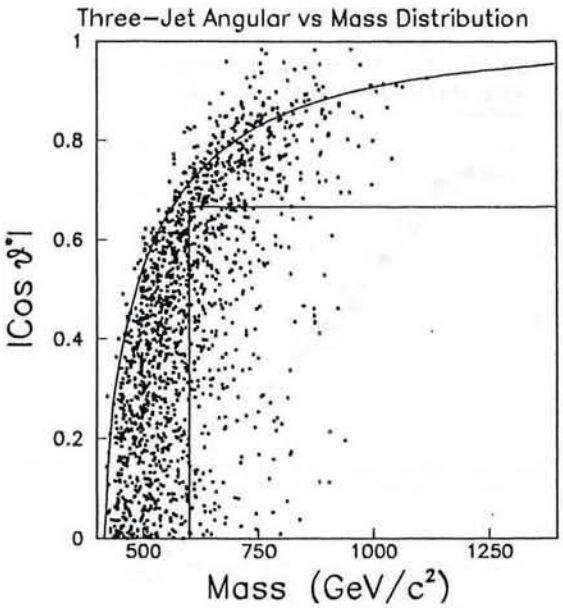

Figure 11: Distribution of $\cos\theta^*$ versus mass for three-jet events. The curve shows, as a function of mass, the maximum value of $\cos\theta^*$ consistent with the minimum $\sum E_T$ requirement. The box shows the region $\cos\theta^* < 0.67$ and $m > 600$ GeV.

6 Exclusive Three-Jet Analysis

We can generalize the two-jet analysis described in the previous section to systems with an arbitrary number of jets N. The relevent mass is now the N-body mass. We define $\cos\theta^*$ to be the angle between the average beam direction and the highest energy jet in the N-body rest frame. Within the framework of QCD, the N-body matrix elements have singularities corressponding to N-jet configurations that approach two-jet configurations. We therefore expect the N-jet $\cos\theta^*$ distributions to be similar to the two-jet angular distribution. Furthermore, to the extent that the shape of the N-jet mass distributions at large mass reflect the rapidly falling parton structure functions, we might also expect similar mass distributions.

The three-jet $\cos\theta^*$ versus mass distribution is shown in Fig. 11. There are 1595 three-jet events of which 308 events (19%) are within the $|\cos\theta^*| < 0.67$ and m > 600 GeV region. It appears that the high-mass and large angle region is still contained within the fully efficient region. However, it should be noted that the expression for $\cos\theta^*_{MAX}$ (equation 12) is only strictly valid for two-jet events. Indeed a close inspection of Fig. 11 reveals that at low mass

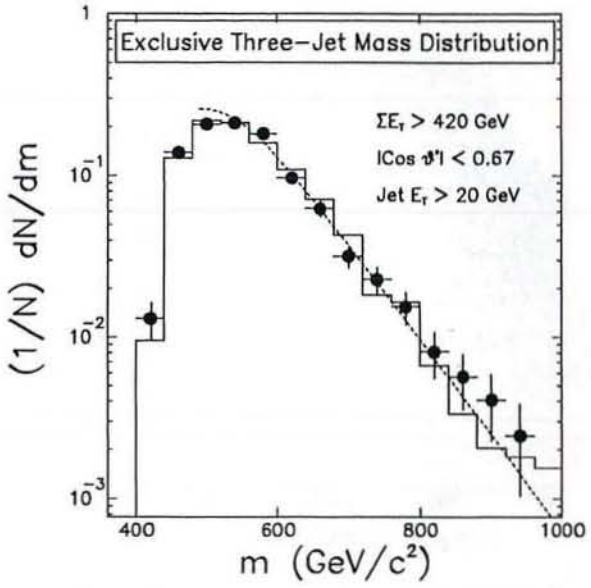

Figure 12: Three-Jet mass distribution. Data (points) compared with HERWIG (histogram) and NJETS (broken line) predictions.

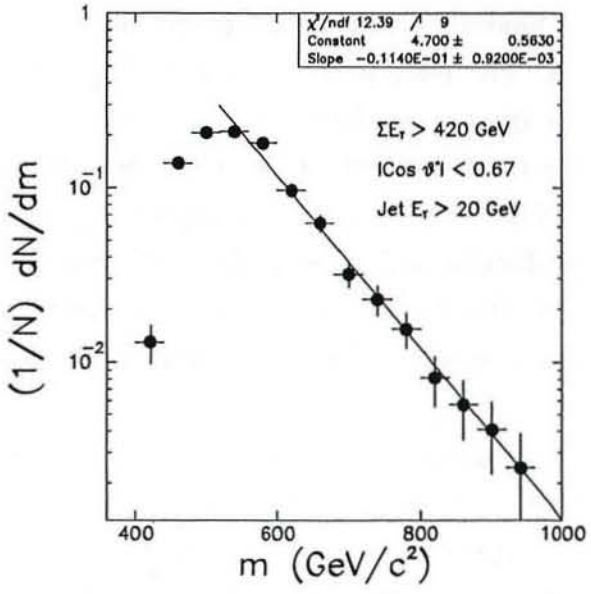

Figure 13: Exponential fit to the exclusive three-jet mass spectrum.

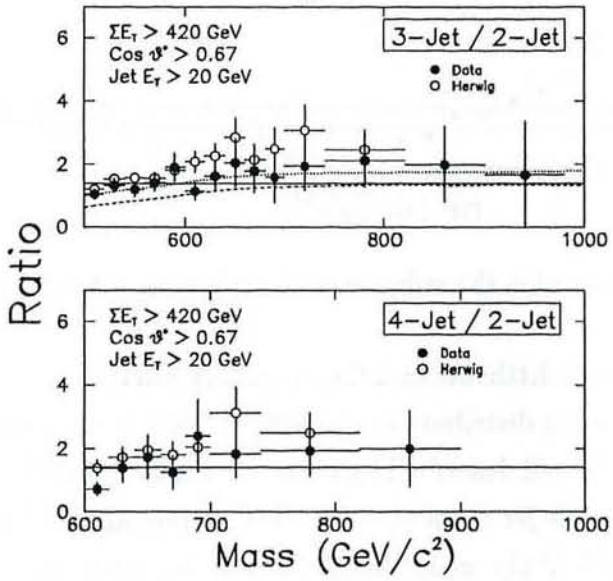

Figure 14: Ratio of two-jet and three-jet rates (top) and ratio of two-jet and four-jet rates (bottom) shown as a function of the multijet mass. Data (closed points) are compared with HERWIG predictions (open points) and NJETS predictions (dotted curve on top plot). As a measure of the uncertainty on the NJETS predictions arising from the details of the jet reconstruction algorithm, the dashed curve on the top plot shows the NJETS prediction for a mimimum jet separation $\triangle R = 1.4$.

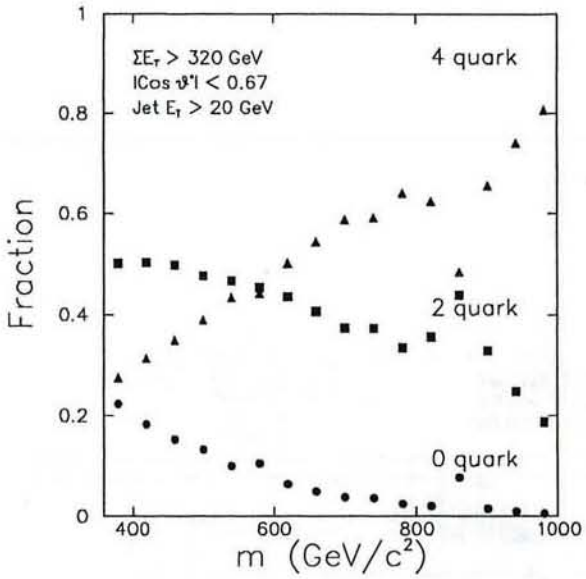

Figure 15: NJETS predictions for the subprocess fractions as a function of three-jet mass.

the inefficient region extends a little beyond the boundary curve.

The observed three-jet mass distribution ($|\cos\theta^*| < 0.67$) is shown in Fig. 12 to extend up to about 1 TeV, and to be well described by both the HERWIG and the NJETS LO QCD predictions. Note that the three-jet mass $m = 600$ GeV, is just above the turn on region, and for masses larger than 600 GeV the mass distribution is described by a simple exponential distribution (Fig. 13), with a slope parameter $b = -0.0114 \pm 0.0009\ GeV^{-1}$. Thus the three-jet mass distribution has a shape at high mass similar to the corressponding two-jet distribution. There is no significant evidence for a deviation from QCD expectations at high mass that can be ascribed to parton-substructure, or exotic resonant three-jet production.

The similarity between the shapes of the two-jet and three-jet mass distributions is clearly exhibited in the ratio of two-jet to three-jet rates as a function of mass (Fig. 14). Both HERWIG and NJETS predict that this ratio of rates does not depend strongly on mass. HERWIG slightly overestimates the magnitude of the two-jet to three-jet ratio, whilst NJETS agrees well with the data. Note that the next-to-leading order (NLO) NJETS calculation is currently available for the $2 \to 2$ process, and the NLO $2 \to 3$ calculation is expected in the future[7]. When this is available we will be able to compare the 3-jet / 2-jet ratio to the NLO predictions.

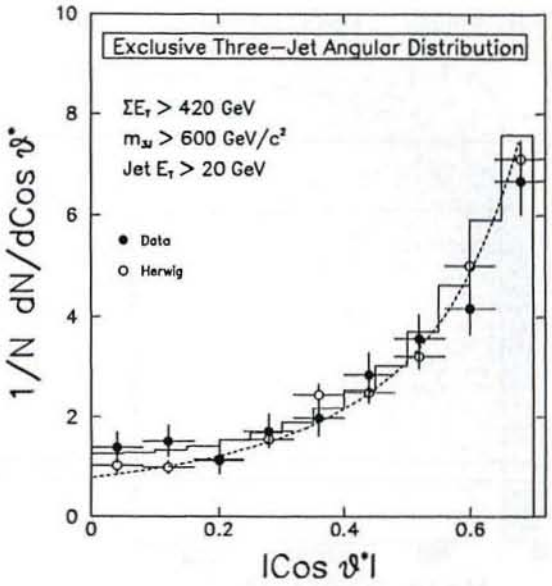

Figure 16: Three-jet angular distribution. Data (solid points) compared with HERWIG (open points) predictions, NJETS (histogram) predictions, and the Rutherford scattering form (broken curve).

The predicted variation with mass of the parton-parton subprocess mix (Fig.15) is similar to the corressponding variation for the two-jet case. Since the subprocess mix varies significantly with mass, the agreement between the observed and predicted three-jet mass distributions provides an indirect check that the relative contributions from the various leading order subprocesses are well described by the theory.

Finally, the three-jet angular distribution (Fig. 16) is similar to the corressponding two-jet distribution and is well described by the HERWIG predictions, the NJETS predictions, and by the Rutherford scattering form.

7 Exclusive Four-Jet Analysis

The four-jet $\cos\theta^*$ versus mass distribution is shown in Fig. 17. There are 1105 four-jet events of which 274 events are within the $|\cos\theta^*| < 0.67$ and m $>$ 600 GeV region. The calculated boundary $\cos\theta^*_{MAX}$ (equation 12) gives a poor description of the edge of the inefficient region. However, it appears that our high-mass and large angle region is still contained within the fully efficient part of the $\cos\theta^*$ versus mass plane, although only just.

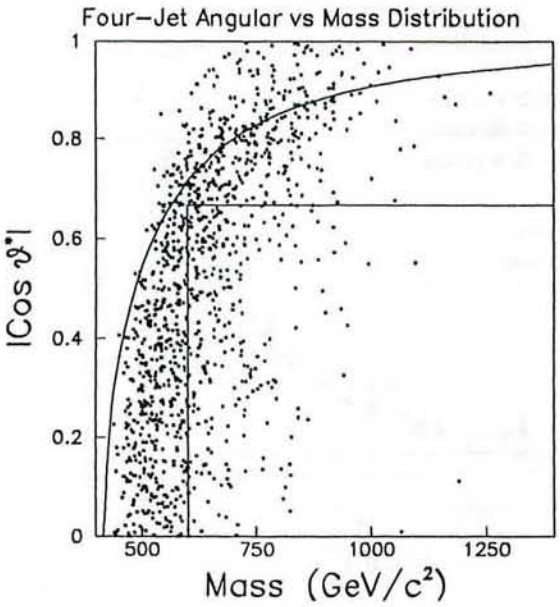

Figure 17: Distribution of $\cos\theta^*$ versus mass for four-jet events. The curve shows, as a function of mass, the maximum value of $\cos\theta^*$ consistent with the minimum $\sum E_T$ requirement. The box shows the region $\cos\theta^* < 0.67$ and $m > 600$ GeV.

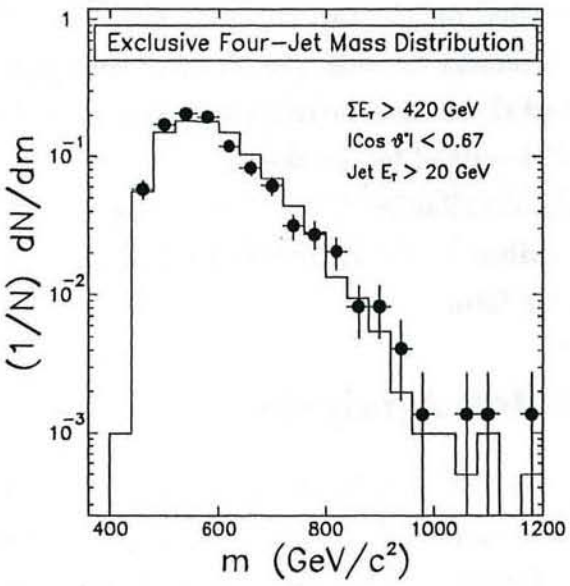

Figure 18: Four-Jet mass distribution. Data (points) compared with HERWIG predictions (histogram).

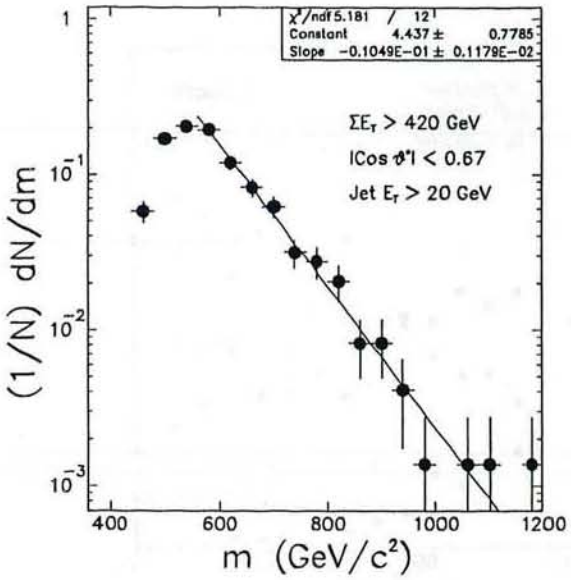

Figure 19: Exponential fit to the exclusive four-jet mass spectrum.

The observed four-jet mass distribution ($|\cos\theta^*| < 0.67$) extends up to masses of 1.2 TeV, and is shown in Fig. 18 to be well described by the HERWIG predictions. NJETS LO QCD calculations are in progress. Once again, for events with $\cos\theta^* < 0.67$, a multijet mass of 600 GeV is (just) above the turn-on region. In the region $m_{4J} > 600$ GeV the four-jet mass distribution is described by a simple exponential distribution (Fig. 19), with a slope parameter $b = -0.0105 \pm 0.0012\ GeV^{-1}$, similar to, but harder than, the corressponding two-jet slope. There is no evidence for an excess of events at high four-jet mass that could be ascribed to resonant four-jet production.

The similarity between the shapes of the two-jet and four-jet mass distributions is clearly exhibited in the ratio of two-jet to four-jet rates as a function of mass (Fig. 14). HERWIG correctly predicts that this ratio of rates does not depend strongly on mass, and is also able to describe the magnitude of the two-jet to four-jet ratio.

The predicted variation with mass of the parton-parton subprocess mix (Fig. 20) is similar to the corressponding variation for the two-jet case. Once again, the agreement between the observed and predicted multijet mass distributions provides some indirect evidence that the contributions from the different leading order subprocesses are correctly predicted by the HERWIG QCD parton shower Monte Carlo.

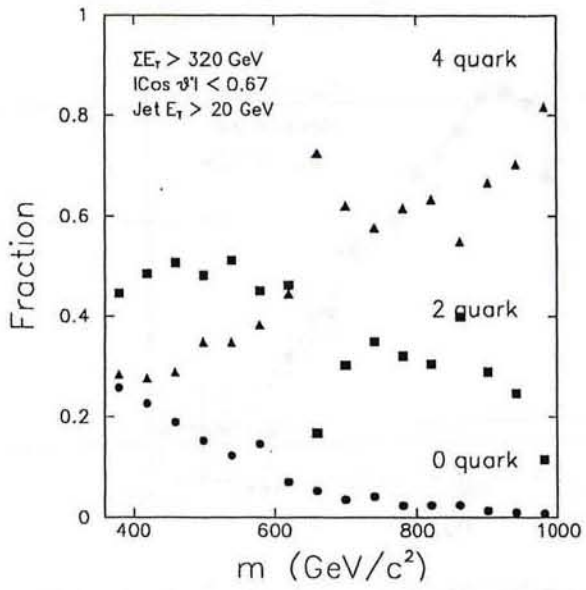

Figure 20: NJETS predictions for the subprocess fractions as a function of four-jet mass.

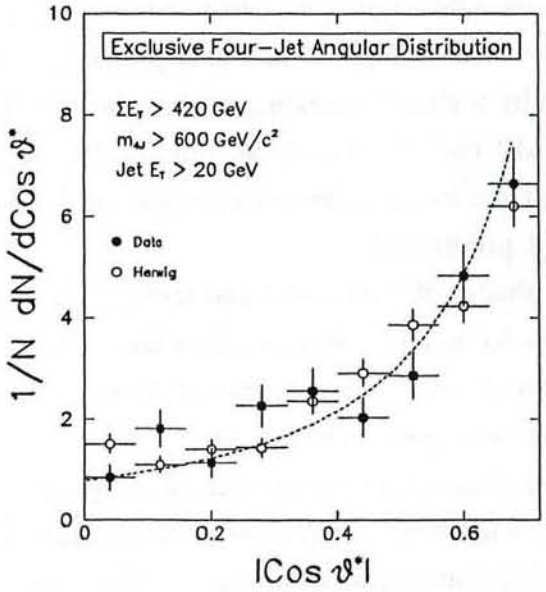

Figure 21: Four-jet angular distribution. Data (solid points) compared with HERWIG predictions (open points), and the Rutherford scattering form (curve).

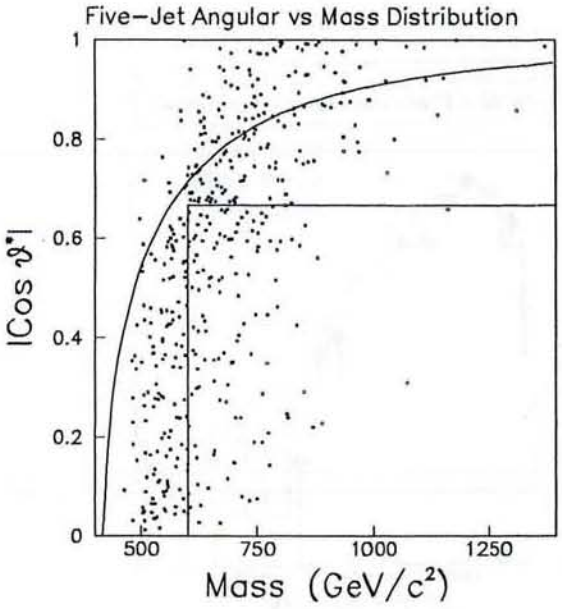

Figure 22: Distribution of $\cos\theta^*$ versus mass for five-jet events. The curve shows, as a function of mass, the maximum value of $\cos\theta^*$ consistent with the minimum $\sum E_T$ requirement. The box shows the region $\cos\theta^* < 0.67$ and $m > 600$ GeV.

The four-jet angular distribution (Fig. 21) is similar to the corressponding two-jet distribution and is well described by both the HERWIG predictions and by the Rutherford scattering form.

8 Exclusive Five-Jet Analysis

The five-jet $\cos\theta^*$ versus mass distribution is shown in Fig. 22. There are 436 five-jet events of which 129 events are within the $|\cos\theta^*| < 0.67$ and m > 600 GeV region. The calculated boundary $\cos\theta^*_{MAX}$ (equation 12) gives a poor description of the edge of the inefficient region. However, it appears that our high-mass and large angle region is still contained within the fully efficient part of the $\cos\theta^*$ versus mass plane, although only just.

The observed five-jet mass distribution ($|\cos\theta^*| < 0.67$) extends up to masses of about 1.2 TeV and is shown in Fig. 23 to be reasonably well described by the HERWIG + QFL predictions in the region above the turn-on. The HERWIG + QFL predictions give a poor description of the turn-on region. Furthermore the mass m = 600 GeV is close to the edge of the turn-on region. We do not at this time have corressponding predictions from the NJETS

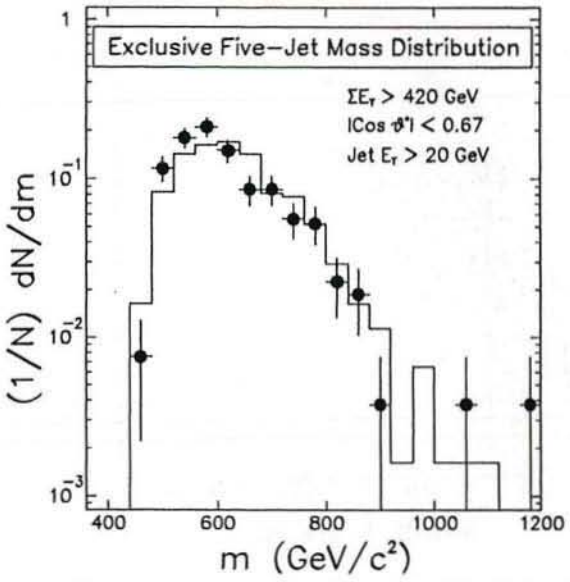

Figure 23: Five-Jet mass distribution. Data (points) compared with HERWIG predictions (histogram).

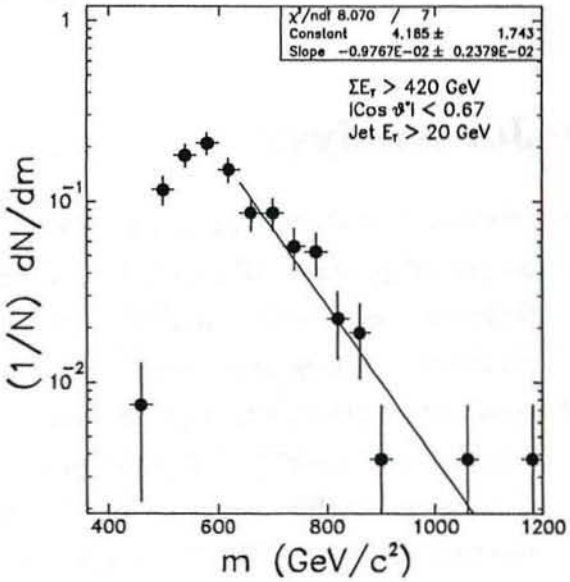

Figure 24: Exponential fit to the exclusive five-jet mass spectrum.

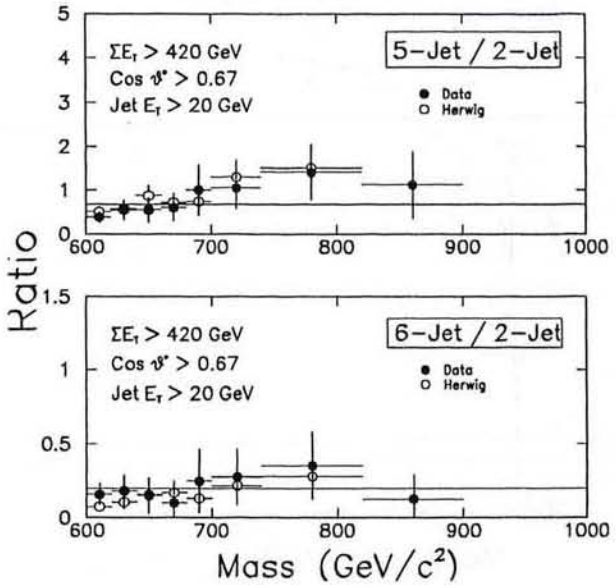

Figure 25: Ratio of two-jet and five-jet rates (top) and ratio of two-jet and six-jet rates (bottom). Data (closed points) are compared with HERWIG predictions (open points).

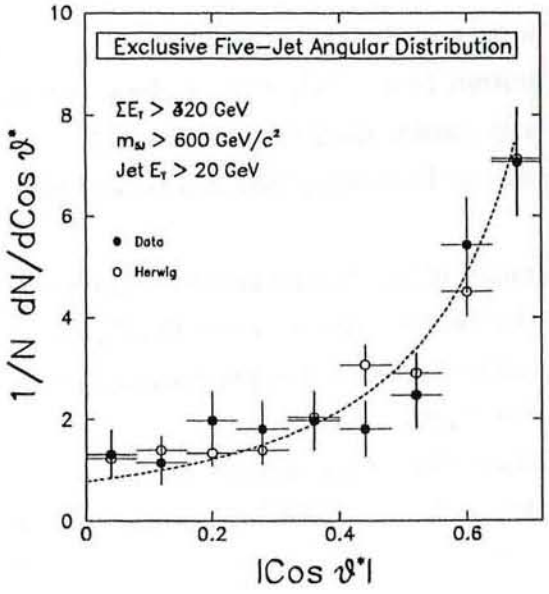

Figure 26: Five-jet angular distribution. Data (solid points) compared with HERWIG (open points) predictions, and the Rutherford scattering form (broken curve).

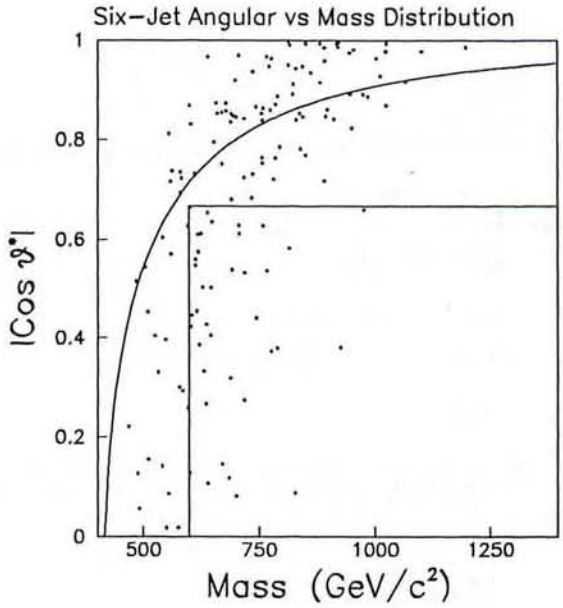

Figure 27: Distribution of $\cos\theta^*$ versus mass for six-jet events. The curve shows, as a function of mass, the maximum value of $\cos\theta^*$ consistent with the minimum $\sum E_T$ requirement. The box shows the region $\cos\theta^* < 0.67$ and $m > 600$ GeV.

program.

At multijet masses above the turn-on (m > 600 GeV) the mass distribution is described by a simple exponential distribution (Fig. 24), with a slope parameter $b = -0.0098 \pm 0.0024\ GeV^{-1}$, similar but slightly harder than the corressponding two-jet slope. There is no evidence for an excess of events at high-mass that can be ascribed to exotic production of multijet systems.

The similarity between the shapes of the two-jet and five-jet mass distributions is clearly exhibited in the ratio of two-jet to five-jet rates as a function of mass (Fig. 25). HERWIG correctly predicts that this ratio of rates does not depend strongly on mass, and is also able to describe the magnitude of the two-jet to five-jet ratio.

The five-jet angular distribution (Fig. 26) is similar to the corressponding two-jet distribution and is well described by both the HERWIG predictions and by the Rutherford scattering form.

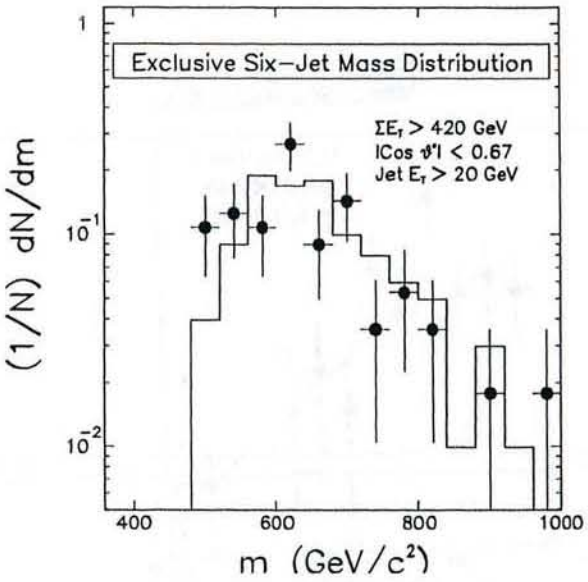

Figure 28: Six-Jet mass distribution. Data (points) compared with HERWIG predictions (histogram).

9 Exclusive Six-Jet Analysis

The six-jet $\cos\theta^*$ versus mass distribution is shown in Fig. 27. There are 141 six-jet events of which 38 events are within the $|\cos\theta^*| < 0.67$ and m > 600 GeV region. The high-mass and large angle region is clearly very close to the edge of the fully efficient region.

The observed six-jet mass distribution ($|\cos\theta^*| < 0.67$) is shown in Fig. 28 to be reasonably well described by the HERWIG + QFL predictions. The $m > 600$ GeV cut is a little below the edge of the fully efficient region. Above the turn-on region the mass distribution is described by a simple exponential distribution (Fig. 29), with a slope parameter $b = -0.0060 \pm 0.0048\ GeV^{-1}$. The similarity between the shapes of the two-jet and six-jet mass distributions is clearly exhibited in the ratio of two-jet to six-jet rates as a function of mass (Fig. 25). HERWIG correctly predicts that this ratio of rates does not depend strongly on mass. However, the HERWIG predictions have a tendency to be slightly lower than the observed two-jet to six-jet ratio. It is possible that this discrepancy arises in part because at six-jet masses of 600 GeV we are still not in the fully efficient region, and the turn-on is not adequately described by the simulation. Unfortunately limited statistics does not permit us to clarify this further.

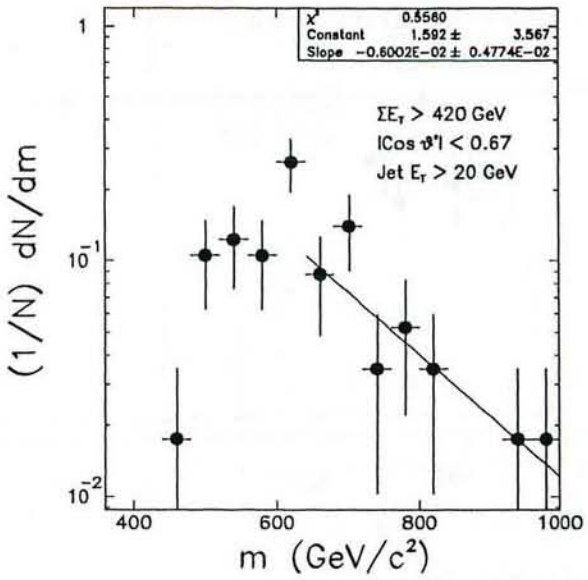

Figure 29: Exponential fit to the exclusive six-jet mass spectrum.

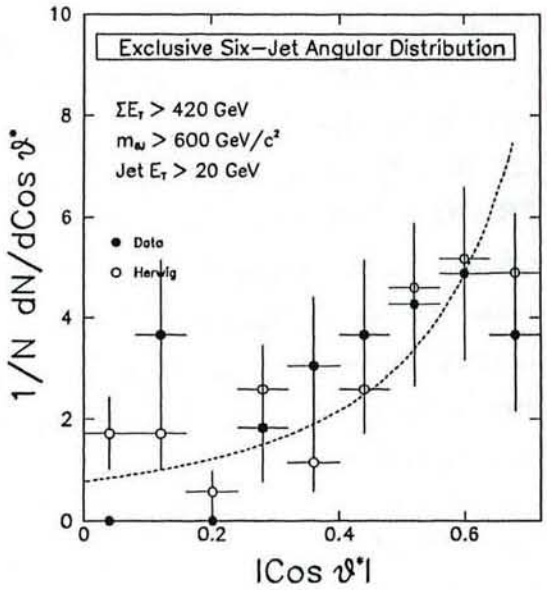

Figure 30: Six-jet angular distribution. Data (solid points) compared with HERWIG (open points) predictions, and the Rutherford scattering form (broken curve).

The six-jet angular distribution (Fig. 30) is similar to the corressponding two-jet distribution and, within the precision of the limited statistics, is well described by both the HERWIG Monte Carlo predictions and by the Rutherford scattering form. It should be noted that the highest $|\cos\theta^*|$ bin falls below the Rutherford scattering curve for both HERWIG and the data. This is a further indication that for $m < 600$ GeV the fully efficient region does not quite extend out to $|\cos\theta^*| = 0.67$.

10 Seven-Jet Events

The seven-jet $\cos\theta^*$ versus mass distribution is shown in Fig. 31. There are 36 seven-jet events of which 8 events are in the large mass and small $\cos\theta^*$ region. Statistics are thus too limited for a detailed comparison with QCD expectations for the mass and angular distributions. However, comparing Fig. 31 with the corressponding six-jet distribution (Fig. 27), the two distributions are similar, at least to the extent that within the very limited statistics there is no evidence for radically different population of events for seven-jet events. We must await more data before we can explore the seven-jet topology in more detail.

Run	Event	Mass(GeV)	$\lvert\cos\theta^*\rvert$	$\sum E_T(GeV)$
40190	74072	646	0.42	522
42427	172979	701	0.47	472
42592	109076	824	0.24	621
42670	60605	949	0.40	587
45089	346457	600	0.16	473
45998	3500	662	0.37	490
46599	43443	642	0.39	432
47753	180952	662	0.45	508

Table 3: The seven-jet events with $|\cos\theta^*| < 0.67$ and $m > 600$ GeV.

The seven-jet events with $\cos\theta^* < 0.67$ and $m > 600$ GeV are listed in Table 3, and have been hand-scanned using the DF display. The subjective conclusions from the scanning are :-

(i) Event 40190-74072: Fairly clean topology with seven well separated clusters. The uncorrected total energy is 621 GeV.

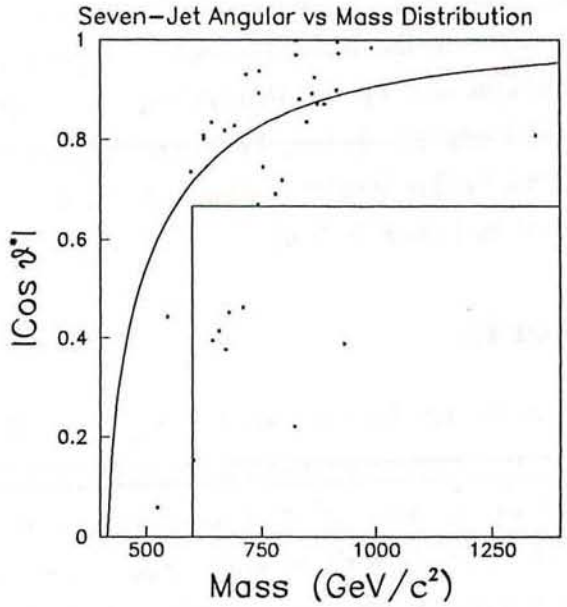

Figure 31: Distribution of $\cos\theta^*$ versus mass for seven-jet events. The curve shows, as a function of mass, the maximum value of $\cos\theta^*$ consistent with the minimum $\sum E_T$ requirement. The box shows the region $\cos\theta^* < 0.67$ and $m > 600$ GeV.

(ii) Event 42427-172979: Fairly clean topology with five well separated clusters plus some additional activity which forms the additional two clusters. The uncorrected total energy is 728 GeV.

(iii) Event 42592-109076: Looks like a two-jet event. The remaining clusters are formed from relatively soft hits widely spread over the calorimeter. The uncorrected total energy is 1005 GeV.

(iv) Event 42670-60605: Three-jet event with some additional relatively soft clusters. The uncorrected total energy is 992 GeV.

(v) Event 45089-346457: Six-jet event with a softer additional cluster formed from some soft hits. The uncorrected total energy is 835 GeV.

(vi) Event 45998-3500: Seven cleanly separated clusters. However the jet algorithm has merged two of them, and made an additional soft clusters out of some softer hits in the plug. The uncorrected total energy is 804 GeV.

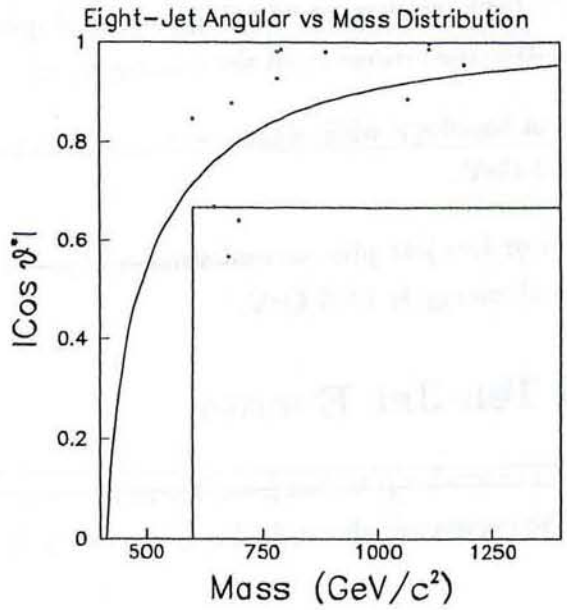

Figure 32: Distribution of $\cos\theta^*$ versus mass for eight-jet events. The curve shows, as a function of mass, the maximum value of $\cos\theta^*$ consistent with the minimum $\sum E_T$ requirement. The box shows the region $\cos\theta^* < 0.67$ and $m > 600$ GeV.

(vii) Event 46599-43443: Three-jet event with the additional clusters coming from scattered softer activity. The uncorrected total energy is 1141 GeV.

(viii) Event 47753-180952: Three-jet event with additional clusters from scattered softer hits. The uncorrected total energy is 663 GeV.

11 Eight-Jet Events

The eight-jet $\cos\theta^*$ versus mass distribution is shown in Fig. 32. There are 14 events with eight jets, of which 2 events have $\cos\theta^* < 0.67$ and $m > 600$ GeV. The event numbers together with the multijet masses and $\cos\theta^*$ are listed in Table 4 for the 2 events with $\cos\theta^* < 0.67$.

Run	Event	Mass(GeV)	$\lvert\cos\theta^*\rvert$	$\sum E_T(GeV)$
42899	417417	662	0.56	533
47617	232706	702	0.64	443

Table 4: The 2 eight-jet events with $\cos\theta^* < 0.67$.

The events in Table 4 have been hand-scanned using the DF display. Event pictures are shown in Fig. 33. The subjective conclusions from the scanning are :-

(i) Event 42899-417417: Clean topology with eight nicely separated clusters. The uncorrected total energy is 961 GeV.

(ii) Event 47617-232706: Four or five jets plus several smaller clusters .. fairly clean topology. The uncorrected total energy is 1356 GeV.

12 Nine-Jet and Ten-Jet Events

The jet multiplicity distribution extends up to ten jets. There are two events with nine jets and one event with ten jets. The events are shown in Figures 33 and 34, and listed in Table 5.

Run	Event	N_J	Mass(GeV)	$\mid \cos\theta^* \mid$	$\sum E_T(GeV)$
43016	6415	9	936	0.985	451
45727	476318	9	829	0.946	511
46697	24405	10	873	0.955	440

Table 5: The ten-jet and 4 nine-jets events.

All of the nine-jet and ten-jet events have multijet masses m $>$ 600 GeV. None of the events have $\mid \cos\theta^* \mid < 0.67$. Nevertheless the events are spectacular. Note that:

(i) Run 43016 Event 6415 is a nine-jet event with total (uncorrected) energy deposition of 1636 GeV, and a poorly defined toplogy. There are three well separated hard clusters and lots of scattered soft hits.

(ii) Run 45727 Event 476318 is a nine-jet event with total (uncorrected) energy deposition of 805 GeV, and a fairly cleanly defined toplogy. It looks like a four-jet event in which two of the jets have been split and the remaining clusters are initiated by softer scattered hits.

(iii) The ten-jet event (Run 46697 Event 24405) has a remarkably clean topology, and the total (uncorrected) energy deposition is 1690 GeV.

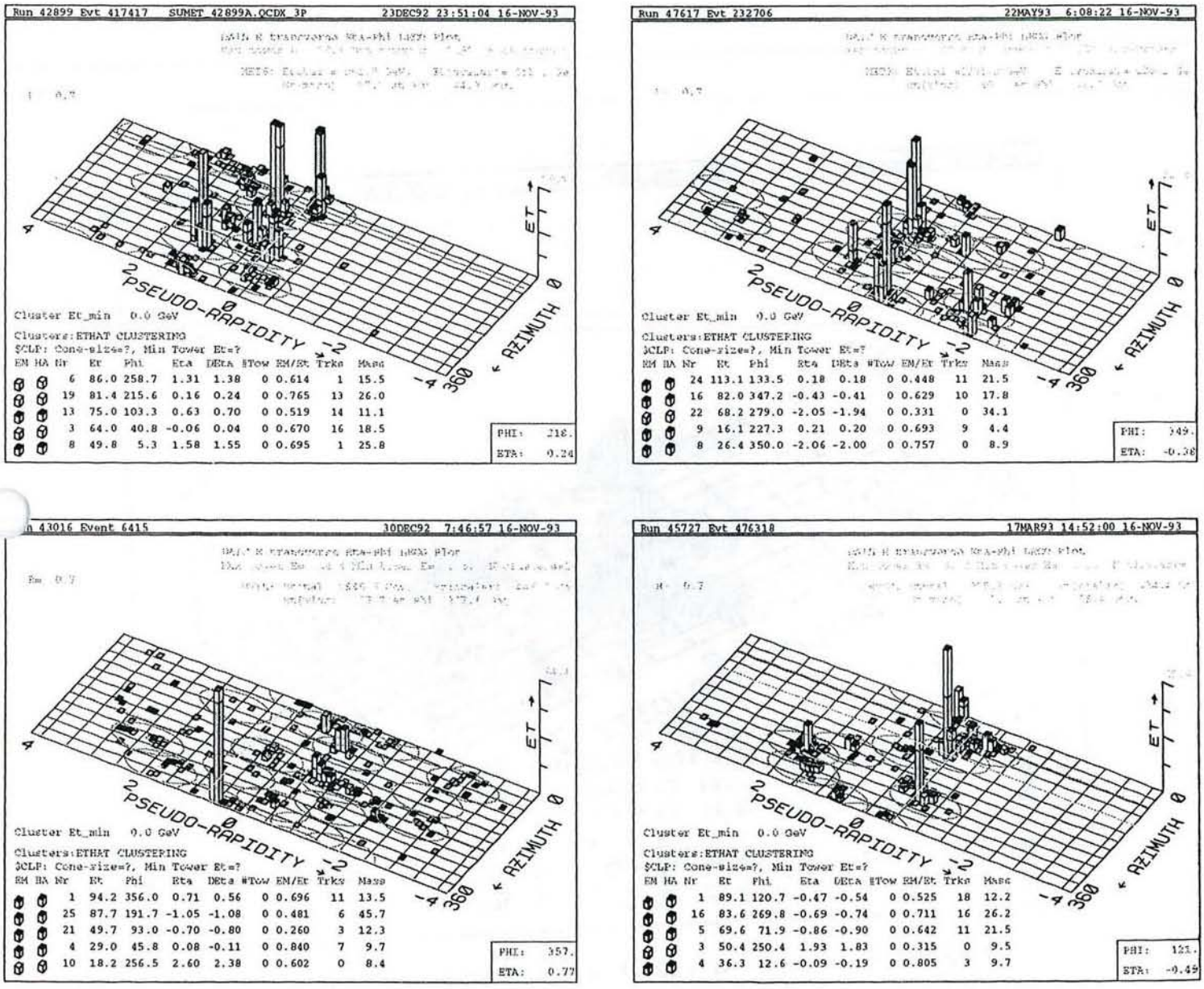

Figure 33: The two 8-jet events with $|\cos\theta^*| < 0.67$ and $m > 600$ GeV (see Table 4), and the two nine-jet events (see Table 5).

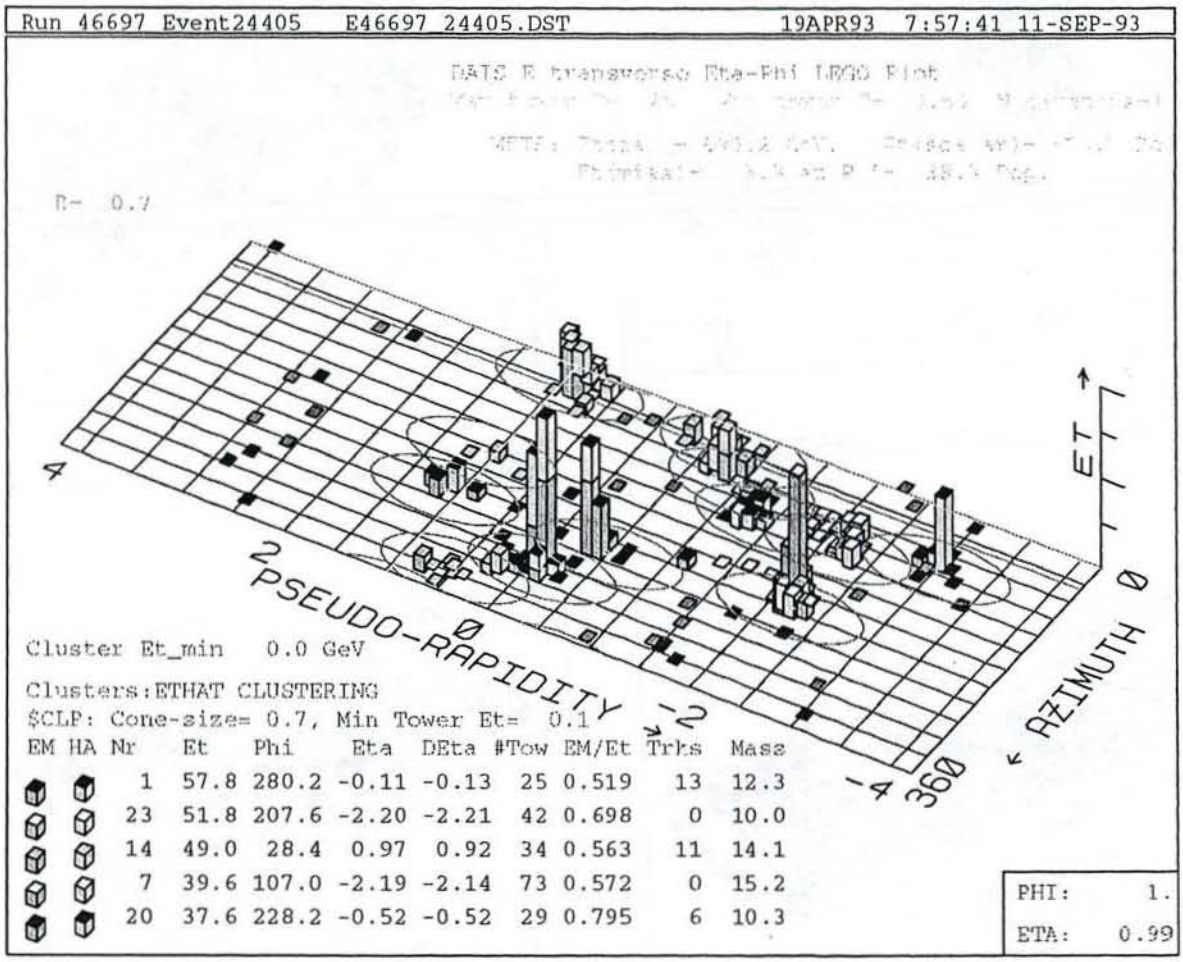

Figure 34: The event with 10 jets with corrected jet $E_T > 20$ GeV.

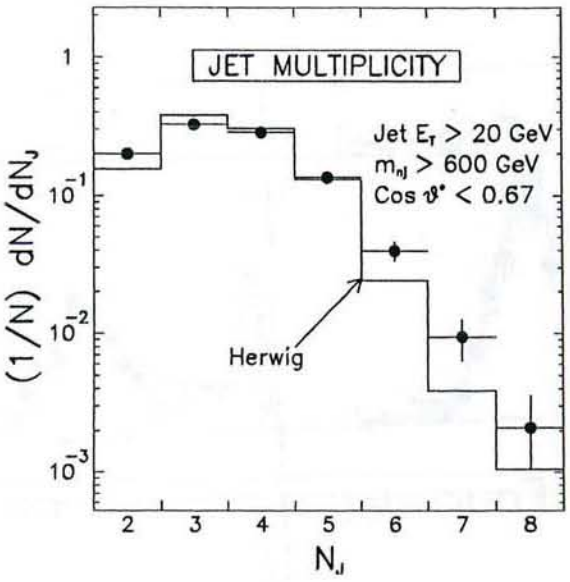

Figure 35: Jet multiplicity distribution for events with m > 600 GeV and $\cos\theta^* < 0.67$. Data (points) compared with HERWIG predictions (histogram). Jets have been reconstructed with a cone size $\triangle\ R = 0.7$ and retained if the corrected jet E_T exceeds 20 GeV.

13 Jet Multiplicity and Transverse Momentum Distributions

In Fig. 4 we saw that although the HERWIG + QFL predictions correctly describe the fraction of events with two-jets, three-jets, four-jets, and five-jets, nevertheless the data show an excess of events for topologies with six or more jets, and the discrepency increases with increasing jet multiplicity. Since for event topologies with four or more jets the turn-on regions of the multijet mass plots are not well described by the Monte Carlo predictions, we restrict ourselves to the region above the turn-on and look again at the jet multiplicity distribution. In Fig. 35 the observed jet multiplicity distribution for events with m > 600 GeV and $\cos\theta^* < 0.67$ is compared with the QCD expectations. The disagreement between data and HERWIG expectations persists. We suspect that this discrepency reflects a limitation of the QCD LO parton shower Monte Carlo.

We noted in section 4 that a similar discrepancy has been reported in a comparison of the W + N-jet complete LO QCD predictions with the corressponding predictions from a QCD parton shower Monte Carlo. In that study it was found that for N > 1 the parton

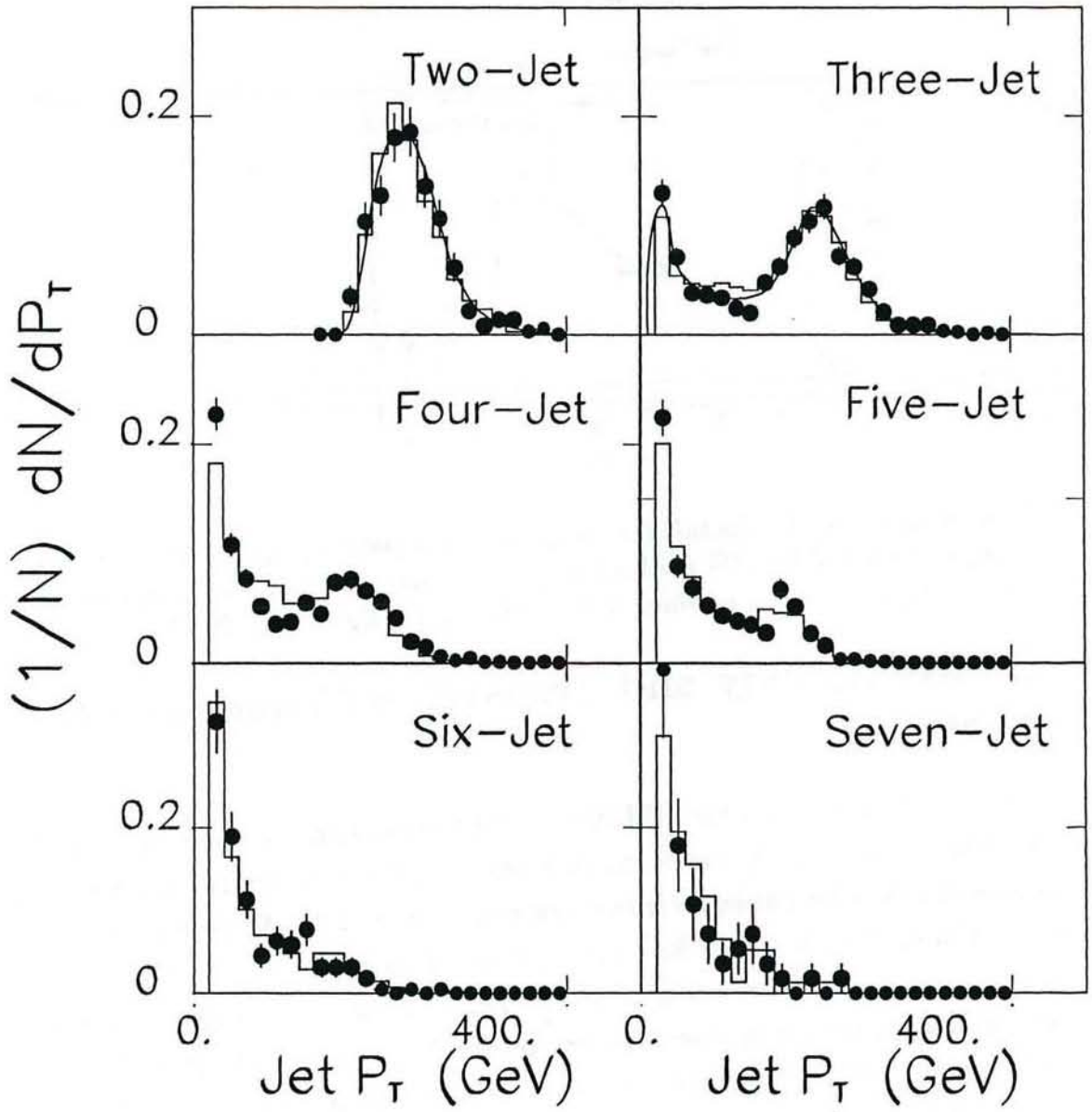

Figure 36: Jet transverse momentum distributions shown as a function of jet topology for events with m $>$ 600 GeV and $\cos\theta^{\star} < 0.67$. Data (points) compared with HERWIG predictions (histogram). Jets have been reconstructed with a cone size $\triangle\ R = 0.7$ and retained if the corrected jet E_T exceeds 20 GeV.

shower Monte Carlo predicted a significantly softer jet transverse momentum distribution than the complete LO calculation. With this in mind, in Fig. 36 we compare data with QCD predictions for the distributions of jet transverse momenta as a function of the jet topology. The jet transverse momentum distribution for two-jet events is well described by the HERWIG Monte Carlo. However, the HERWIG descriptions of the three-jet and four-jet distributions are poor; the predicted shapes of the soft part of the spectra seem to be too hard. On the other hand NJETS, the full LO $2 \rightarrow$ N calculation, is seen to give an adequate description of the two-jet and three-jet jet-transverse-momentum distributions. This may indicate that the full LO $2 \rightarrow$ N calculation provides a better description than HERWIG of the multijet kinematics. Perhaps events with large total transverse energies and several jets in the final state probe the QCD matrix element at a level deeper than that of the parton shower Monte Carlo approximation.

Finally we note that within the limited statistical precision of the data sample, HERWIG gives a resonable description of the jet transverse momentum distributions for events with five or more jets. Higher statistics samples in the future should enable us to see if discrepancies at the level observed for the three-jet and four-jet distributions are also present when there are five or more jets in the final state.

14 Conclusions

The Jet multiplicity distribution for events with $\sum E_T > 420$ GeV extends up to multiplicities of 10. Hand scanning reveals that even with ten jets in the event, the event topologies are often well defined, and the data quality appears to be good with only an occassional event ascribable to a detector malfunction. Statistics are sufficient to compare in some detail the multijet mass and angular distributions for topologies with up to six jets in the final state. The main conclusions from the study described in this note are:

(1) Angular Distributions: At high multijet masses the angular distributions for the hardest jet in the N-body rest frame are all similar to the Rutherford scattering form and are well described by the HERWIG + QFL parton shower model QCD predictions, and, where available, by the full LO $2 \rightarrow$ N matrix element calculation NJETS.

(2) Mass Distributions: In the region above the turn on ($\cos\theta^* < 0.67$ and $m > 600$ GeV) the multijet mass distributions for events with large total transverse energy are well

described by our QCD predictions: HERWIG + QFL, and where available, the NJETS LO calculation. The mass distributions are also well described by an exponentially falling distribution. Fit results are listed in Table 6 for the N-jet mass distributions. Note that the two-jet, three-jet, four-jet, five-jet, and six-jet mass-distributions have similar fitted slope parameters which perhaps show evidence for a slow hardening of the multijet mass spectra with increasing jet multiplicity.

Topology	Slope	Fit χ^2
2	-0.0135 ± 0.0011	0.99
3	-0.0114 ± 0.0009	1.38
4	-0.0105 ± 0.0012	0.43
5	-0.0098 ± 0.0024	1.15
6	-0.0060 ± 0.0048	0.56

Table 6: Fit results from the exponential fits to the multijet mass distributions, fitted in the region above the turn on.

(3) The Turn-On Region: Except for the two- and three-jet mass distributions, the turn-on regions of the multijet mass distributions are not well described by the HERWIG + QFL Monte Carlo. This perhaps indicates an inadequacy of the detector simulation.

(4) Jet Multiplicity Distribution: The QCD parton shower Monte Carlo gives a reasonable description of the fraction of events with two-, three-, four-, and five-jets, but underestimates the event rate at higher jet multiplicities. This discrepancy increases with increasing jet multiplicity. Although we suspect that this reflects a limitation of the QCD parton shower Monte Carlo, it is not at present fully understood.

(5) Jet Transverse Momentum Distributions: The QCD parton shower Monte Carlo gives a reasonable description of the jet transverse momentum distributions for two-jet events, but does not give an adequate description for three-jet or four-jet events. The full LO matrix element calculation NJETS gives a good description of the jet transverse momentum distributions for two-jet and three-jet events .. thus perhaps we are probing the QCD matrix element beyond the parton-shower Monte Carlo approximation. Statistics are still too limited to see if there is also a descrepency between data and HERWIG predictions for the jet transverse momentum distributions in events with five or more jets.

15 Acknowledgements

Many thanks to Walter Giele for the NJETS predictions that appear throughout this note. The analysis described in this note is a part of a broader analysis of the properties of events with large total transverse energies. In that context the expressline total E_T data sample and the HERWIG Monte Carlo sample were prepared by Liz Buckley-Geer. The trigger we implemented in the 1992-3 run was developed from work done in collaboration with Chris Wendt, and grew out of our analysis of the 1988-9 data samples.

References

[1] A Study of Events with the Highest Total Transverse Energy in CDF, E. Buckley and S. Geer; *CDF/PUB/JET/PUBLIC/2160, FERMILAB-CONF-93/208E* (1993).

[2] F. Abe et al. (CDF Collaboration), *Phys. Rev.* **D45**, 1448 (1992).

[3] F. Abe et al. (CDF Collaboration), *Phys. Rev. Lett.* **62**, 1825 (1989).

[4] G. Marchesini and B. Webber, *Nucl. Phys.* **B310**, 461 (1988).

[5] F. Abe et al. (CDF Collaboration), *Phys. Rev.* **D45**, 2249 (1992).

[6] W. Giele et al; Snowmass 1990 Proceedings, page 137.

[7] W. Giele, private communication.